Dynamics of laboratory models of the wind-driven ocean circulation

Andrew Elek Kiss

A thesis submitted for the degree of
Doctor of Philosophy
of The Australian National University.

Research School of Earth Sciences

December 2000

Except where otherwise indicated in the text, the research described in this thesis is my own original work.

Andrew E. Kiss
15th December 2000

Acknowledgements

I would like thank my supervisor Prof. Ross Griffiths for his advice and support throughout this study. I have also benefited greatly from many discussions with Prof. George Veronis regarding the numerical and theoretical aspects of this work. I gratefully acknowledge the helpful advice offered by many of the participants in the 1998 WHOI Summer Program in GFD, especially Drs. Steve Meacham, Bill Young, Drew Poje, Mike Shelley and Neil Balmforth. I also express my gratitude to Assoc. Prof. Michael Page for generously making his code available for this research.

It has been a pleasure to work in the friendly atmosphere the GFD Group. Mathew Wells in particular has always been great company.

Many thanks to those noble souls (Mum, Dad, Prof. Ross Griffiths and Dr. Ross Kerr) who helped with the proof-reading. Thanks also to Mum, Dad and Sandra Hatch for all their practical support.

Finally, a big thank-you to Sarah for her love, support and patience.

Abstract

This thesis presents a numerical exploration of the dynamics governing rotating flow driven by a surface stress in the "sliced cylinder" model of Pedlosky & Greenspan (1967) and Beardsley (1969), and its close relative, the "sliced cone" model introduced by Griffiths & Veronis (1997). The sliced cylinder model simulates the barotropic wind-driven circulation in a circular basin with vertical sidewalls, using a depth gradient to mimic the effects of a gradient in Coriolis parameter. In the sliced cone the vertical sidewalls are replaced by an azimuthally uniform slope around the perimeter of the basin to simulate a continental slope. Since these models can be implemented in the laboratory, their dynamics can be explored by a complementary interplay of analysis and numerical and laboratory experiments.

In this thesis a derivation is presented of a generalised quasigeostrophic formulation which is valid for linear and moderately nonlinear barotropic flows over large-amplitude topography on an f-plane, yet retains the simplicity and conservation properties of the standard quasigeostrophic vorticity equation (which is valid only for small depth variations). This formulation is implemented in a numerical model based on a code developed by Page (1982) and Becker & Page (1990).

The accuracy of the formulation and its implementation are confirmed by detailed comparisons with the laboratory sliced cylinder and sliced cone results of Griffiths (Griffiths & Kiss, 1999) and Griffiths & Veronis (1997), respectively. The numerical model is then used to provide insight into the dynamics responsible for the observed laboratory flows. In the linear limit the numerical model reveals shortcomings in the sliced cone analysis by Griffiths & Veronis (1998) in the region where the slope and interior join, and shows that the potential vorticity is dissipated in an extended region at the bottom of the slope rather than a localised region at the east as suggested by Griffiths & Veronis (1997, 1998). Welander's thermal analogy (Welander, 1968) is used to explain the linear circulation pattern, and demonstrates that the broadly distributed potential vorticity dissipation is due to the closure of geostrophic contours in this geometry.

The numerical results also provide insight into features of the flow at finite Rossby number. It is demonstrated that separation of the western boundary current in the sliced cylinder is closely associated with a "crisis" due to excessive potential vorticity dissipation in the viscous sublayer, rather than insufficient dissipation in the outer western boundary current as suggested by Holland & Lin (1975) and Pedlosky (1987*b*). The stability boundaries in both models are refined using the numerical results, clarifying in particular the way in which the western boundary current instability in the sliced cone disappears at large Rossby and/or Ekman number. A flow regime is also revealed in the sliced cylinder in which the boundary current separates without reversed flow, consistent with the potential vorticity "crisis" mechanism. In addition the location of the stability boundary is determined as a function of the aspect ratio of the sliced cylinder, which demonstrates that the flow is stabilised in narrow basins such as those used by Beardsley (1969, 1972,

1973) and Becker & Page (1990) relative to the much wider basin used by Griffiths & Kiss (1999).

Laboratory studies of the sliced cone by Griffiths & Veronis (1997) showed that the flow became unstable only under anticyclonic forcing. It is shown in this thesis that the contrast between flow under cyclonic and anticyclonic forcing is due to the combined effects of the relative vorticity and topography in determining the shape of the potential vorticity contours. The vorticity at the bottom of the sidewall smooths out the potential vorticity contours under cyclonic forcing, but distorts them into highly contorted shapes under anticyclonic forcing. In addition, the flow is dominated by inertial boundary layers under cyclonic forcing and by standing Rossby waves under anticyclonic forcing due to the differing flow direction relative to the direction of Rossby wave phase propagation. The changes to the potential vorticity structure under strong cyclonic forcing reduce the potential vorticity changes experienced by fluid columns, and the flow approaches a steady free inertial circulation. In contrast, the complexity of the flow structure under anticyclonic forcing results in strong potential vorticity changes and also leads to barotropic instability under strong forcing.

The numerical results indicate that the instabilities in both models arise through supercritical Hopf bifurcations. The two types of instability observed by Griffiths & Veronis (1997) in the sliced cone are shown to be related to the western boundary current instability and "interior instability" identified by Meacham & Berloff (1997*b*). The western boundary current instability is trapped at the western side of the interior because its northward phase speed exceeds that of the fastest interior Rossby wave with the same meridional wavenumber, as discussed by Ierley & Young (1991).

Numerical experiments with different lateral boundary conditions are also undertaken. These show that the flow in the sliced cylinder is dramatically altered when the free-slip boundary condition is used instead of the no-slip condition, as expected from the work of Blandford (1971). There is no separated jet, because the flow cannot experience a potential vorticity "crisis" with this boundary condition, so the western boundary current overshoots and enters the interior from the east. In contrast, the flow in the sliced cone is identical whether no-slip, free-slip or super-slip boundary conditions are applied to the horizontal flow at the top of the sloping sidewall, except in the immediate vicinity of this region. This insensitivity results from the extremely strong topographic steering near the edge of the basin due to the vanishing depth, which demands a balance between wind forcing and Ekman pumping on the upper slope, regardless of the lateral boundary condition. The sensitivity to the lateral boundary condition is related to the importance of lateral friction in the global vorticity balance. The integrated vorticity must vanish under the no-slip condition, so in the sliced cylinder the overall vorticity budget is dominated by lateral viscosity and Ekman friction is negligible. Under the free-slip condition the Ekman friction assumes a dominant role in the dissipation, leading to a dramatic change in the flow structure. In contrast, the much larger depth variation in the sliced cone leads to a global vorticity balance in which Ekman friction is always dominant, regardless of the boundary condition.

Contents

List of Figures

Chapter 1

Introduction

1.1 Overview

At mid-latitudes the large-scale mean horizontal circulation of the upper 1 – 2 km of the global ocean is dominated by subtropical and subpolar gyres driven by the surface wind stress. These gyres are recirculations spanning the width of ocean basins, with slow meridional flow in most of the basin returned by narrow, rapid boundary currents at the western side. These currents separate from the coast at some point and meander across the interior between the gyres. Western-intensified circulations of this type appear at mid-latitudes in all ocean basins, examples of the poleward western boundary current being the Gulf Stream in the North Atlantic, the Kuroshio in the North Pacific and the East Australia Current in the South Pacific. Subtropical and subpolar gyres have a similar western-intensified form, but subtropical gyres have an anticyclonic circulation, whilst subpolar gyres are cyclonic.

The wind-driven mid-latitude circulation forms an important part of the global climate system. The western boundary currents of subtropical gyres transport warm water poleward from equatorial regions, whilst those of subpolar gyres carry cold polar water equatorward. The resulting sea surface temperature anomalies and the effects they have on evaporation have a profound influence on the climate of neighbouring continental regions. For instance, Europe is warmed by the extension of the Gulf Stream, whilst Newfoundland is cooled by the Labrador current. Separated western boundary currents generally coincide with frontal boundaries, where the outcropping of isopycnals to the surface results in strong lateral density and temperature gradients. The temperature contrast across these subpolar fronts also has a strong influence on the local climate. The energetic flow in western boundary current separation regions is highly variable on timescales of a few years to a few decades, and this variability is thought to be an important factor in climate fluctuations (Plaut *et al.*, 1995).

This thesis presents a numerical study of laboratory models of the wind-driven general circulation characteristic of midlatitude subtropical or subpolar gyres.

1.2 Background

From the point of view of fluid dynamics, understanding the behaviour of the global ocean is an immensely complex problem. There are processes operating on spatial scales ranging from millimetres to tens of thousands of kilometres, and timescales from seconds to millennia. The fluid is rotating, stratified, turbulent, contained within a domain with a highly irregular boundary and subject to forcing which is generally unpredictable in

both space and time. The complex physics leads to a plethora of different wave modes and instabilities, and highly nonlinear motions are common. In addition the motions and properties of the ocean and atmosphere are intimately linked, leading to coupled modes of variability such as El Niño and the Antarctic Circumpolar Wave.

To make progress in analysing or modelling aspects of the ocean circulation it is clearly necessary to make simplifications, chosen to yield a tractable problem while retaining the essential physics of the processes of interest. This thesis is concerned with the horizontal, upper-ocean component of the general circulation at mid-latitudes; thus only motions with a horizontal scale of order 100 km or more, and timescales of order months and longer will be considered. Veronis (1973*a*) discusses in detail the simplifications made in order to study this flow. A brief overview of some of these is given below.

The "β-plane"

Large-scale horizontal circulation is strongly affected by both the Coriolis "force" due to the rotation of the Earth, and its variation with latitude due to the Earth's curvature. When the latitudinal scale of the motion is not too large, the "β-plane" approximation is often made, by which the curvature of the Earth is neglected except insofar as it affects the Coriolis term, which is considered to have a linear dependence on latitude.

Stratification

The density stratification of the oceans strongly influences the dynamics of large-scale ocean circulation, by allowing baroclinic (depth-dependent) motions to exist in addition to the barotropic (depth-independent) motions which occur with homogeneous density. In particular, stratification allows the flow to become baroclinically unstable, producing the energetic mesoscale eddies which are prevalent at mid-latitudes. In addition, stratification changes the timescales of the flow, since the baroclinic component of the circulation takes about a decade to adjust to changes in wind forcing, in marked contrast to the barotropic adjustment timescale of a few weeks (Rhines, 1986). The density structure of the oceans is also thought to be a crucial factor in determining the path of subsurface flow (Rhines & Young, 1982*b*).

The density typically varies slowly as a function of depth in the surface mixed layer, increases rapidly through the pycnocline and then increases very slowly with depth in the deep ocean (Levitus, 1982). A two-layer approximation to this stratification is often made, which models the surface and deep layers as homogeneous and the pycnocline as a sharp interface between them, typically at a depth of several hundred metres. If the flow in the upper layer is of primary interest, a "1.5-layer" approximation is often made, which simplifies the dynamics further by assuming the lower layer is motionless. It is also common to neglect stratification entirely, by depth-averaging the flow so that only the barotropic component is included.

Forcing

Atmospheric forcing of the oceans occurs largely through the influence of surface pressure and wind stress, and through buoyancy fluxes due to heating, evaporation and precipitation. It is thought that the horizontal gyral circulation of the upper ocean is primarily wind-driven, whilst a combination of buoyancy and wind stress drives the slow vertical circulation and deep abyssal flow which establishes the stratification of the oceans (Harrison, 1989; Peixoto & Oort, 1992). Although in reality these motions are inextricably

combined to produce the actual ocean circulation (McWilliams, 1996), it is common practice to consider purely wind-driven motion in a basin with a given stratification, while neglecting the much slower processes which maintain the density structure.

The surface wind stress is highly variable, and on large space scales and time scales of more than a few days its fluctuating component is best described as a stochastic field with white spatial and temporal spectra (Frankignoul & Müller, 1979). The only significant spectral variations are a power-law fall-off in energy for periods shorter than three days (Willebrand, 1978), and peaks at periods of 6 and 12 months, and possibly at longer inter-annual periods corresponding to events such as El Niño (Harrison, 1989). These spectral peaks occur to different degrees in different geographical locations. Although nonlinear rectification of transient forced motion may affect the mean flow (Griffa & Castellari, 1991; Griffa & Salmon, 1989; Pedlosky, 1965*b*; Veronis, 1966*a*, 1970), it is generally assumed that the basic features of the mean circulation can be studied by including only the steady component of the wind forcing. This approach focuses attention on intrinsic (rather than forced or coupled) modes of variability. It was shown by Sverdrup (1947) that the *curl* of the wind stress is crucial in driving large-scale flow; its time average is anticyclonic over subtropical gyres and cyclonic over subpolar gyres (Hellerman & Rosenstein, 1983; Trenberth *et al.*, 1990), which accounts for the differing sense of circulation in these gyres.

Topography, basin shape and inter-basin flow

The topography of the ocean floor and its intersection with the surface (the coastline) can also exert a strong influence on the general circulation, possibly controlling such important aspects as the point of separation of western boundary currents from the coast (Dengg, 1993; Pedlosky, 1965*a*). There are also many significant flows between oceans, such as the Antarctic Circumpolar Current which links all southern oceans, the Indonesian Throughflow from the western Pacific into the northeastern Indian ocean, and the flow of the Agulhas current from the southern Indian ocean into the South Atlantic.

Given that many of the gross features of mid-latitude gyres (slow equatorward interior flow, rapid poleward western boundary current, et cetera) are similar in all ocean basins, we can presumably understand these features without including geographical details of particular basins such as the bottom topography, basin shape, and inter-basin flow. It is therefore common in process studies to use a very simple geometry such as a rectangular basin with a flat bottom, containing only one or two gyres (determined by the form of the wind stress). The effects of inter-basin flow are usually neglected by specifying no flow through the basin boundaries.

Dissipation

Turbulence extends to spatial scales much smaller than those of interest in the general circulation, and indeed much finer than the grid resolution which is practical to use in numerical general circulation models. Since these fine scales cannot be explicitly included it is necessary to parameterise the effects of turbulence on the large-scale flow.

Turbulent small-scale oceanic motion is usually presumed to mix momentum and scalars in a way that appears similar to diffusion when viewed at much larger scales (although the "best" form of the diffusion operator is the subject of continuing debate). Thus for basin-scale flows the relevant viscosity is not molecular viscosity, but the "eddy viscosity" by which the small-scale turbulence is parameterised. Since turbulent mixing is restricted in the vertical direction due to stratification, there are different kinematic eddy

viscosities in the vertical and horizontal directions. The actual values are very poorly constrained, estimates for the vertical and horizontal kinematic eddy viscosities being 10^2 – 10^5 and 10^7 – 10^{10} times the molecular value, respectively (Pedlosky, 1987*a*; von Schwind, 1980). As a result the eddy viscosities are often treated as free parameters which are "tuned" in order to obtain realistic results, or simply to ensure numerical stability. Although a reasonable first approximation, the use of a fixed eddy viscosity is problematic, since in reality it is due to small-scale dynamics which vary in space and time (Pedlosky, 1971).

Dissipation of gyre-scale motion occurs through both lateral and bottom turbulent stresses. Eddy viscosity plays an insignificant part in gyre flows except where there is strong shear, such as in western boundary currents and the upper and lower Ekman boundary layers. Although the flow outside these regions can be considered essentially inviscid, its motion is due to the "viscous" dynamics of the wind-driven upper boundary layer.

The use of a lateral diffusion term to model small-scale turbulence raises the mathematical order of the governing differential equations, and requires that higher-order boundary conditions be specified. If the dissipation were due to molecular viscosity there is no question that the no-slip condition is appropriate for solid boundaries. However, since the diffusion is the assumed effect of small to mesoscale turbulent eddies it can be argued (Pedlosky, 1996) that the effect of the boundary on nearby eddies will reduce the flux through the boundary of along-shore momentum, and that a more "slippery" boundary condition should be used, such as partial-slip, free-slip (no stress), "super-slip" (no vorticity flux) or "hyper-slip" (no potential vorticity flux).

1.3 Overview of theory

Our understanding of the dynamics which control the wind-driven circulation has been built up over many decades by the complementary interplay of observation and analytical, numerical and laboratory modelling. Although ocean general circulation models are routinely used to simulate the circulation in realistic ocean basins (or even the global ocean), simplified analytical and numerical models continue to play an important role in isolating and clarifying the fundamental processes at work in the general circulation. These models typically employ a simple rectangular basin with no topography or inter-basin flow, and simplify or omit the stratification. The wind stress is usually steady, with a highly idealised spatial structure chosen to produce only one or two gyres. The dynamics are often simplified by making the quasigeostrophic approximation. This minimalist approach yields insight into the intrinsic, generic dynamics which are not dependent on the details of the forcing or the geometry of a particular ocean basin. In addition to clarifying the dynamics, the relative simplicity of such models often results in computational efficiency, making it practical to produce long time series and conduct detailed surveys of the dependence of the flow on various parameters (such as the wind strength or the strength of the dissipation). Idealised process models thus yield a detailed understanding of the fundamental dynamics governing oceanic flows which is impractical to obtain from general circulation models due to their complexity and computational expense.

The basic features of the wind-driven circulation are captured by barotropic models. Despite their very simple formulation, the behaviour of these models can be richly complex, particularly when the flow is strongly inertial; the physics of barotropic models therefore remains the subject of active research. The processes which operate in the real oceans must be at least as complex as those in idealised barotropic models, so an understanding

of these can be regarded as a necessary first step towards understanding oceanic flows.

Early theory

The first major theoretical advance on this topic was made by Sverdrup (1947), who showed that at large scales the depth-averaged circulation will be driven across lines of latitude by the surface wind stress curl. The time-averaged wind stress has anticyclonic curl over subtropical gyres and cyclonic curl over subpolar gyres (Hellerman & Rosenstein, 1983; Trenberth *et al.*, 1990), resulting in an equatorward Sverdrup transport in subtropical gyres and poleward flow in subpolar gyres.

Stommel (1948) and Munk (1950) derived simple linear models of flow in basins with no topography and showed (respectively) that bottom friction or lateral viscosity can break the Sverdrup balance at the western boundary to allow a return flow of the interior transport in a narrow (and therefore rapid) western boundary current. These models provided the first dynamical explanation of this ubiquitous feature of midlatitude circulation. A very different analytical model was developed by Fofonoff (1954), in which the interior flow recirculates via inertial boundary layers against all boundaries, and both forcing and dissipation are absent.

Pioneering numerical investigations into the inertial modification of the Munk and Stommel models were carried out by Bryan (1963) and Veronis (1966*b*), respectively (thus Bryan's model had lateral friction but no bottom friction, while the opposite was true for Veronis' model). At moderate Reynolds number both models displayed northward intensification of the western boundary current, and the outflow extended along the northern boundary for a short distance. At large Reynolds number the western boundary current outflow in Bryan's model separated from the northern boundary and flowed around the perimeter of a localised recirculation in the northwestern corner before entering the interior. The flow also became unstable, displaying a train of northward-propagating disturbances in the western boundary current upstream of the recirculation. In contrast, the flow in Veronis' model did not become unstable at large Reynolds number. Instead of separating in the northwest, the western boundary current extended along the northern boundary and entered the interior from the east, forming a large recirculating cell whose transport far exceeded that predicted by Sverdrup theory.

Sensitivity to boundary conditions

Further numerical experiments by Blandford (1971) showed that when both bottom and lateral friction are present the strongly nonlinear circulation resembles that in either Bryan's or Veronis' model, depending on whether the lateral boundary condition is no-slip or free-slip, respectively. This pointed to the crucial role played by the choice of lateral boundary conditions in determining the gross qualitative behaviour of the flow at large Reynolds number. The sensitivity to boundary conditions has been demonstrated in more detail in later investigations (Dengg, 1993; Haidvogel *et al.*, 1992; Moro, 1988), and it has been shown that even subtle details of the numerical implementation can be important in the no-slip case (Verron & Blayo, 1996). This sensitivity is rather alarming, since the appropriate lateral boundary condition at the coast is a subject of continuing debate.

Western boundary layer breakdown and recirculation

The formation of a compact recirculation gyre in the northwest has been related to the breakdown of the boundary-layer approximation when the boundary current outflow must

be matched to a sufficiently rapid eastward Sverdrup flow (Ierley, 1987; Ierley & Ruehr, 1986). The dynamics which drive the recirculation itself have been investigated by Cessi *et al.* (1987), Ierley & Young (1988) and Cessi (1990). The related "inertial runaway" seen by Veronis (1966*b*) at large Reynolds number has been studied by Briggs (1980), Harrison & Stalos (1982), Merkine *et al.* (1985), Böning (1986), Verron & Jo (1994), Cessi & Ierley (1995) and Ierley & Sheremet (1995) in various models with free-slip boundary conditions.

Western boundary current separation

The question of what processes control the separation of western boundary currents has attracted significant attention over the years, particularly because inaccurate prediction of the separation site has been a persistent problem in ocean general circulation models (McWilliams, 1996). Among the factors which have been shown to influence separation in particular models are a change in sign of the wind stress curl (Munk, 1950), a collision with another western boundary current (Agra & Nof, 1993; Cessi, 1991), a region of "adverse" longshore pressure gradient (Baines & Hughes, 1996; Haidvogel *et al.*, 1992), the requirement of potential vorticity balance (Verron & Le Provost, 1991), outcropping of isopycnals (Parsons, 1969; Veronis, 1973*b*) or a change in bottom topography or boundary shape (Dengg, 1993; Greenspan, 1963; Özgökmen *et al.*, 1997; Pedlosky, 1965*a*; Spitz & Nof, 1991). That so many factors can play a part (at least in principle) suggests that the actual separation process in the oceans is very complex indeed.

Instability

The physics responsible for the onset of instability has also been studied extensively using simplified models. The barotropic western boundary current instability first observed by Bryan (1963) has been analysed in terms of viscous instability theory by Ierley & Young (1991), and this theory was extended to the case of an inclined coastal boundary by Cessi & Ierley (1993). The analysis of this type of instability has also been generalised to 1.5 and two-layer quasigeostrophic flows by Berloff & Meacham (1998) and to three-layer quasigeostrophic flows by Berloff & McWilliams (1999*b*). Additional modes of instability have also been identified in barotropic (Le Provost & Verron, 1987; Meacham & Berloff, 1997*b*; Moro, 1990; Sheremet *et al.*, 1997, 1995), 1.5-layer (Berloff & McWilliams, 1999*a*; Berloff & Meacham, 1998; Dijkstra & Katsman, 1997; Dijkstra & Molemaker, 1999; Speich *et al.*, 1995) and two-layer flows (Berloff & McWilliams, 1999*a*; Berloff & Meacham, 1998). The mode of instability which first appears is dependent on the physics included in the model (e.g. whether it includes stratification) and also on the choice of parameters such as the basin size and shape. At parameters well beyond the initial onset of instability the time-dependence typically becomes very complex, and ultimately chaotic. The transitions leading to the onset of chaos have been investigated in several different models, using the techniques of dynamical systems theory (Berloff & Meacham, 1997; Jiang *et al.*, 1995; Meacham & Berloff, 1997*a*; Sheremet *et al.*, 1995).

Continental slopes

There has recently been a resurgence of interest in the role of continental slope topography in modifying the flow in the classical Stommel and Munk models (e.g. Becker, 1995, 1999; Becker & Salmon, 1997; Griffiths & Veronis, 1997, 1998; Kubokawa & McWilliams, 1996; Salmon, 1992). These studies have been motivated both by a need to better understand the role of topographic steering in determining the path of western boundary currents, and by

a hope that the inclusion of this steering will eliminate the sensitive dependence on lateral boundary conditions found in models with vertical sidewalls, since the western boundary current becomes isolated from the western boundary if the depth changes continuously to zero at the coast.

Holland (1967) conducted one of the earliest investigations of this problem, using a single-gyre circulation in a basin with a shallow western region and deeper eastern region joined by a linear slope. He used both numerical solutions of the governing vorticity equation and a generalisation of the Sverdrup relation to show that the flow is guided along contours of constant potential vorticity and is therefore deflected from the path it would take in a flat-bottomed basin to form an equatorward "tail" extending to the southwest. With this topography the fluid is essentially stagnant in a "shadow zone" to the north and west of the potential vorticity contour which intersects the northern boundary at the bottom of the slope. This shadow zone grows southward as the western region is made shallower, and ultimately reaches the southern boundary. At this point the wind-driven gyre becomes confined to the eastern part of the slope and recirculates without encountering the western boundary. An important contribution to this early work was the analogy recognised by Welander (1968) between the vorticity equation for depth-averaged inertia-less flow over topography and the two-dimensional advection-diffusion equation for a passive scalar. This analogy (discussed in section 5.1.3) provides a very useful framework for developing an intuitive understanding of the effects of topography on wind-driven flow.

Welander's approach was revisited after two decades by Salmon, who generalised the analogy to inertia-less two-layer and continuously stratified flows (Salmon, 1992, 1998, respectively). Salmon (1992) used the planetary geostrophic equations to study the limiting case of vanishing depth in the western region, so the fluid depth decreased continuously to zero at the western boundary and the gyre was isolated from the western boundary by the shadow zone. His analysis showed that the form of the streamfunction on the slope is determined by the geometry of the potential vorticity contours and the relationship between the streamfunction and potential vorticity established by the Sverdrup balance in the region of constant depth. Viscous dissipation of potential vorticity is required in order to close the Sverdrup circulation, but in the limit of small friction the dissipation is confined to a thin boundary layer on the slope in the southwest corner of the basin. In this limit the flow on the slope is therefore independent of the value of the friction coefficient, except in this frictional boundary layer. Further theoretical analysis of the influence of a western continental slope on the linear circulation was undertaken by Kubokawa & McWilliams (1996), who determined the way in which the equatorward "tail" shortens as the slope is steepened (or the friction increased), until the flow returns to the familiar Stommel or Munk solution in the limit of large slope and/or friction.

Numerical studies by Becker & Salmon (1997) and Becker (1995, 1999) extended these results into the nonlinear regime and showed that the steering of double-gyre western boundary currents by the western continental slope produces a vorticity distribution which is much more prone to barotropic instability than in the case of vertical sidewalls.

Sensitivity to boundary conditions arises from the requirement that each fluid parcel in a steady flow must dissipate the potential vorticity imparted to it by the wind so that the net change in potential vorticity around a closed streamline is zero. In a flat-bottomed basin with vertical sides the dissipation takes place in a boundary current against the western sidewall, so the side boundary conditions play a crucial role in the basin-integrated vorticity balance. The situation is very different in a basin in which the depth goes smoothly to zero at the boundaries (as in the real ocean), since this aligns ambient

potential vorticity contours with the shoreline in coastal regions. As shown by Kubokawa & McWilliams (1996), the resulting topographic steering acts to keep the boundary currents away from the shore, and it is anticipated (and shown in section 5.3) that this will reduce the importance of boundary conditions at the shore in determining the interior flow at large Reynolds number.

1.4 Laboratory models

Laboratory modelling has been involved in many of the developments in this field as a complementary approach to theory and numerical experimentation which provides a convincing physical demonstration of the processes at work. Although it is possible to directly simulate the β effect in the laboratory (Baker & Robinson, 1969), a more practical alternative is to exploit the dynamical equivalence between β and a depth gradient. This is the approach taken in the "sliced cylinder" model of a wind-driven midlatitude gyre introduced by Pedlosky & Greenspan (1967). The apparatus consists of a cylindrical basin rotating with angular speed Ω, filled with water and bounded above by a rigid horizontal lid and below by a sloping planar base which provides a potential vorticity gradient (see figure 2.1 (a) on p. 12). The fluid is driven by the lid, which rotates at a speed $\epsilon\Omega$ relative to the basin and thereby simulates a uniform wind stress curl. The molecular viscosity of the fluid simulates the eddy viscosity in the large-scale ocean circulation. The dimensionless parameters controlling the flow are the Rossby number $Ro = |\epsilon|$, the Ekman number E, the bottom slope s and the basin aspect ratio. Pedlosky & Greenspan (1967), Greenspan (1969) and Beardsley (1969) analysed this model in the limit $Ro \to 0$, using a perturbation expansion in the bottom slope. Their analysis demonstrated that the circulation is intensified at the west when $s \gg E^{\frac{1}{2}}$, with a topographic Sverdrup balance in the interior and a western boundary current whose lowest-order equations of motion are analogous to those governing the Stommel (1948) or Munk (1950) models, depending on whether $E^{\frac{1}{2}} \ll s \ll E^{\frac{1}{4}}$ or $s \gg E^{\frac{1}{4}}$, respectively (see section 2.2.2 for more details).

Beardsley (1969) investigated this model in the laboratory, and the idea has been followed up in further experimental, analytical and numerical studies (Beardsley, 1972, 1973, 1975; Beardsley & Robbins, 1975; Becker & Page, 1990). For sufficiently small values of the Rossby number the observed flow was consistent with the linear analytical solution for the interior flow (Beardsley, 1969). The experiments and numerical solutions for the sliced cylinder showed that for larger Rossby numbers the western boundary current intensified in the downstream direction. The outflow became increasingly localised to a narrow jet which meandered before merging with the interior. The jet was accompanied by an intense recirculating gyre. When the forcing was sufficiently strong the jet became unstable, periodically shedding eddies which were carried to the west around the outer edge of the recirculation. The recirculation, meanders and onset of instability are all characteristic features seen in numerical models of a single gyre with lateral friction and no-slip boundary conditions (e.g. Blandford, 1971).

All of the sliced cylinder experiments and computations referred to above used "deep" systems having width-to-height ratio of order one. This allowed the relative depth variation across the basin to be kept small, accommodating comparison with linearised analyses at weak forcing. However, the width of the boundary current was not small compared to the width of the basin, so the velocity reversal between the interior Sverdrup flow and the return boundary current occurred at around one half of the cylinder radius, and the eddy structures in unstable flows filled much of the basin. Thus these models were not wide systems like the ocean basins, and perhaps not the most suitable for investigation

of nonlinear phenomena since the behaviour of the unstable jet was constrained by its proximity to the sidewalls.

Whether the boundary current dynamics are dominated by lateral or bottom friction, its dimensional width is determined by the depth of the cylinder, the Ekman number and the bottom slope (Beardsley, 1969). Since there are practical restrictions on the latter two parameters, a laboratory model in which the boundary current occupies a small proportion of the basin is most easily obtained by reducing the depth of the sliced cylinder in relation to its width. This was the approach taken by Griffiths (1995). Laboratory experiments with this shallow sliced cylinder revealed a second transition at very strong forcing which had not been reported before, from periodic to aperiodic eddy shedding.

Laboratory models akin to the sliced cylinder apparatus have found application in modelling the circulation around islands (Helfrich *et al.*, 1999; Pedlosky *et al.*, 1997), the response to time-dependent wind forcing (Beardsley, 1975; Krishnamurti, 1981) and two-layer wind-driven circulation (Griffiths & Cornillon, 1994; Krishnamurti, 1981; Krishnamurti & Na, 1978). A variant of the sliced cylinder has also been developed by Griffiths & Veronis (1997) to investigate of the effect of sloping sidewalls on homogeneous wind-driven flow on a simulated β-plane. In this "sliced cone" model the vertical sidewalls of the sliced cylinder are replaced by an azimuthally uniform slope around the perimeter of the basin so that the fluid depth decreases continuously to zero at the lateral boundary (see figure 2.1 (b) on p. 12). Griffiths & Veronis (1997) undertook a laboratory study of the flow in this apparatus as a function of Rossby and Ekman number and found considerable differences from the flow in the otherwise equivalent sliced cylinder of Griffiths (1995). In the geostrophically guided geometry of the sliced cone, the slow interior flow is encircled by a much faster flow on the slope, leading to a much larger transport than with vertical sidewalls. At large Rossby number the sloping sidewall produces a dramatic asymmetry between flows under cyclonic and anticyclonic forcing. With anticyclonic forcing, the slope introduces a new mode of instability in the western boundary current in addition to the jet instability seen in the sliced cylinder. In contrast, flows with cyclonic forcing were stable under all conditions, even for Rossby numbers far in excess of that required to produce instability in the sliced cylinder. A subsequent paper (Griffiths & Veronis, 1998) presented an analysis of the flow in this model in the linear limit based on an expansion in half-powers of the Ekman number E on the slope and in the interior, with a Stewartson $E^{\frac{1}{4}}$ layer at the junction between these regions to make the azimuthal velocity continuous.

1.5 This thesis

This thesis presents the results of numerical simulations of flow in the sliced cylinder and sliced cone models, which reveal in detail the linear and nonlinear dynamics responsible for the flow observed in the laboratory by Griffiths (Griffiths, 1995; Griffiths & Kiss, 1999) and Griffiths & Veronis (1997). A generalised quasigeostrophic formulation is derived which is valid for linear and moderately nonlinear barotropic flows over $O(1)$ topography on an f-plane. A numerical model of the flow in the sliced cylinder and sliced cone was implemented using this formulation by modifying a code originally developed by Page (1982) and Becker & Page (1990). Detailed comparisons of the numerical and laboratory results are used to verify the accuracy of the formulation and its numerical implementation.

The numerical results provide an understanding of the flows in terms of quantities such as the potential vorticity which are not accessible to laboratory measurement. The numerical model allows a more detailed exploration of the regime boundaries as a function of Ekman and Rossby number, and is also used to explore the dependence of the flow on

the aspect ratio of the sliced cylinder in order to connect the laboratory results of Griffiths with previous work with deeper sliced cylinders (e.g. Beardsley, 1969, 1972, 1973; Becker & Page, 1990). The numerical model is used to test the linear theory of flow in the sliced cone given by Griffiths & Veronis (1998), and to extend theoretical understanding of the flow into the nonlinear regime to provide an explanation of the intriguing dependence of stability on the sign of the wind forcing. The numerical results also clarify the nature of the instabilities found in these models and the potential vorticity dynamics responsible for western boundary current separation. In addition the numerical model of the sliced cone reveals the influence of continental slope topography in reducing the sensitivity of nonlinear flow to the choice of boundary conditions at the shore.

Chapter 2 presents the theoretical background to the project, and provides a derivation of the formulation used and an overview of its implementation in the numerical model. The numerical results from modelling the sliced cylinder and sliced cone flows are presented in Chapters 3 and 4, respectively, and compared in detail with the laboratory results of Griffiths (Griffiths & Kiss, 1999) and Griffiths & Veronis (1997) in order to validate the numerical model. An analysis of the numerical results is given in Chapter 5, which reveals the dynamics responsible for many of the phenomena observed in the laboratory under both linear and nonlinear conditions. Conclusions are presented in Chapter 6. Appendices A and B provide further details on Ekman layer theory and the numerical method, respectively, and a glossary of symbols is given in Appendix C.

Much of the work presented here has either been published or is under review. Chapter 3 is based on Griffiths & Kiss (1999), Chapter 4 is based on Kiss (2000) and many of the ideas presented in Chapter 5 appeared in Kiss & Griffiths (1998) and Kiss (2000).

Chapter 2

Models and theory

2.1 The sliced cylinder and sliced cone

Figure 2.1 shows the "sliced cylinder" apparatus used by Griffiths & Kiss (1999) (hereafter GK99) and the "sliced cone" apparatus employed by Griffiths & Veronis (1997) (hereafter GV97). Both laboratory models are completely filled with water and bounded above by a rigid horizontal lid. The base and sidewall rotate with a constant angular velocity $\Omega\hat{\mathbf{k}}$ about a vertical axis, whilst the rigid lid has a slightly different angular velocity $(1+\epsilon)\,\Omega\hat{\mathbf{k}}$ in order to simulate a spatially uniform wind stress curl.

The sliced cylinder has vertical sidewalls and a planar bottom boundary; we conducted experiments with depth gradients of 0.1 and 0.15[1]. In contrast, the base of the sliced cone has the geometric form of an ungula: the sidewall has a 45° slope relative to the horizontal and this cone is intersected at the top by the horizontal lid and at the bottom by a plane with slope 0.1 which forms the central part of the bottom boundary. Figure 2.1 (b) shows that in the sliced cone geometry the geostrophic contours (contours of constant depth) are circles near the rim and D-shaped curves when they cross the interior. All geostrophic contours are closed curves, in contrast to the sliced cylinder in which all geostrophic contours are blocked by the vertical sidewalls. The potential vorticity gradient imposed by the shallow slope in the interior is analogous to the potential vorticity gradient on a β-plane and allows us to identify directions in the apparatus with various points of the compass (e.g. the shallow end is "north", as shown in the figure; note that the apparatus rotates in the northern hemisphere sense, i.e. $\Omega > 0$). Both models used by GK99 and GV97 had a depth H_o at the centre of 12.5 cm; the width $2a$ was 98.0 cm for the sliced cylinder and 97.3 cm for the sliced cone.

2.2 Theory

Previous numerical studies of the sliced cylinder (Beardsley, 1972, 1973; Beardsley & Robbins, 1975; Becker & Page, 1990; Page, 1981, 1982) have followed the approach of Greenspan (1969) and employed a perturbation expansion in the bottom slope to derive a simplified vorticity equation for the interior flow. This approach is obviously not valid for the sliced cone, since the sidewall slope is $O(1)$ and the depth vanishes at the lateral boundary. A vorticity equation applicable to both the sliced cone and sliced cylinder models is derived in section 2.3. The approximations employed in the derivation are based

[1]GK99 obtained the latter in the laboratory by imposing a slope of 0.05 to the lid in addition to the bottom slope of 0.1 (in this case the lid rotated around an axis normal to its plane).

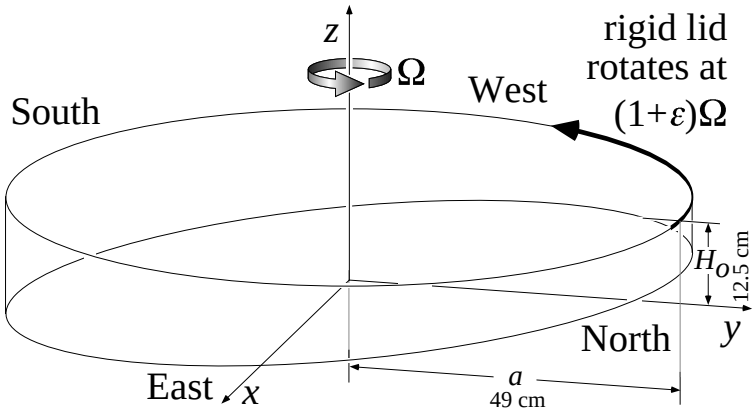

(a) The "sliced cylinder" model

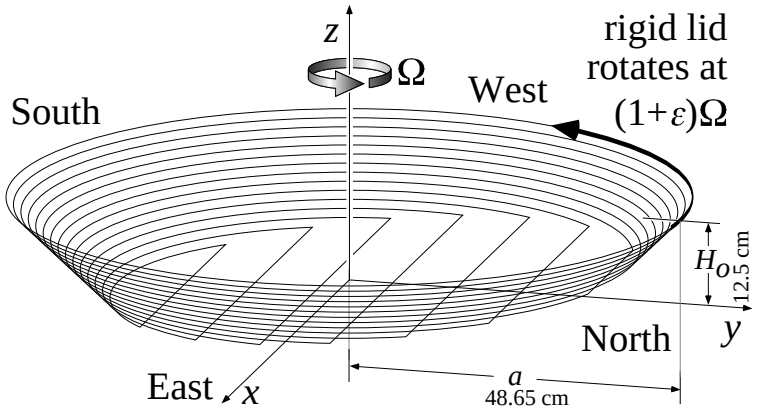

(b) The "sliced cone" model

Figure 2.1: Perspective diagrams of the "sliced cylinder" (a) and "sliced cone" (b) models used in the laboratory and numerical experiments. The compass directions are defined in terms of the potential vorticity gradient imposed by the sloping bottom in the interior. The curves in (b) are contours of constant depth (geostrophic contours).

on scaling arguments presented in the following sections.

There will be an unfortunate profusion of symbols introduced in the following pages; a quick reference to the most important definitions is provided in the glossary of symbols on page 141.

We begin with the Navier-Stokes equations for an incompressible fluid of uniform density, relative to coordinates rotating with constant angular velocity $\Omega\hat{\mathbf{k}}$. These are the momentum equation

$$Ro\left[\frac{\partial \mathbf{u}}{\partial t} + (\mathbf{u}\cdot\nabla)\,\mathbf{u}\right] + 2\hat{\mathbf{k}}\times\mathbf{u} = -\nabla p + E\nabla^2\mathbf{u} \tag{2.1}$$

and continuity equation

$$\nabla\cdot\mathbf{u} = 0, \tag{2.2}$$

where $\mathbf{u}$ is the velocity, p is the pressure and $\hat{\mathbf{k}}$ is the unit vector in the z direction (vertical). We do not include gravitational or centrifugal accelerations since there is no free surface and no stratification; thus the pressure has no hydrostatic or centrifugal components. The length, time, velocity and pressure have been scaled by H_o, $|\epsilon\Omega|^{-1}$, $|\epsilon\Omega|H_o$ and $|\epsilon|\Omega^2 H_o^2\rho$, respectively, where H_o is the depth at the centre of the basin and ρ is the density of the fluid (all quantities introduced in this thesis have been scaled in this way unless otherwise noted). The importance of advection and viscosity are parameterised by the Rossby number $Ro = |\epsilon|$ and Ekman number $E = \frac{\nu}{\Omega H_o^2}$, respectively, where ν is the kinematic viscosity of the fluid. The scaled radius of the tank is $\Lambda = \frac{a}{H_o}$, which will also be referred to as the aspect ratio. With this scaling the radius of the ellipse separating the sloping sidewall and the interior of the sliced cone is given by

$$r_e(\theta) = \frac{\Lambda s_s - 1}{s_s - s_i\sin\theta}, \tag{2.3}$$

where $s_i = 0.1$ is the slope in the interior, $s_s = 1$ is the slope of the sidewall and θ is the azimuthal angle from the x axis (i.e. "due east"). The circle with radius $r_{e_{max}} = r_e(\frac{\pi}{2}) = \frac{\Lambda s_s - 1}{s_s - s_i}$ separates the regions of circular and D-shaped depth contours. With this scaling the top and bottom boundaries are at $z = 1$ and $z = h(x, y)$, respectively, where $h(0, 0) = 0$.

We are interested in the parameter ranges $0 < Ro < 0.2$, $10^{-5} < E < 10^{-3}$ and $\Lambda \approx 4$ corresponding to those used in the experiments of GV97 and GK99. We aim to derive equations governing the flow in the bulk of the fluid, outside the thin ($O(E^{\frac{1}{2}})$) Ekman layers on the top and bottom boundaries. To this end it is convenient to separate the vertical and horizontal components of the velocity by writing $\mathbf{u} = \mathbf{u}_{_H} + \hat{\mathbf{k}}w$, where $\hat{\mathbf{k}}\cdot\mathbf{u}_{_H} = 0$. Without loss of generality the horizontal velocity $\mathbf{u}_{_H}$ can be expressed in terms of a streamfunction ψ and a scalar potential ϕ as

$$\mathbf{u}_{_H} = \mathbf{u}_{_\psi} + \nabla_{_H}\phi, \tag{2.4}$$

where $\mathbf{u}_{_\psi} = \hat{\mathbf{k}}\times\nabla_{_H}\psi$ is the horizontally nondivergent component of the horizontal velocity and $\nabla_{_H}$ is the horizontal gradient operator. With this notation the continuity equation (2.2) becomes $\frac{\partial w}{\partial z} = -\nabla_{_H}^2\phi$.

2.2.1 Steady, linear flow at large scale

In order to obtain an understanding of the characteristics of this flow (in particular the extent to which $\mathbf{u}_{_H}$ is depth-independent and horizontally nondivergent) we will first

consider the steady, linear case, for which the momentum equation (2.1) becomes

$$2\hat{\mathbf{k}} \times \mathbf{u} = -\nabla p + E\nabla^2 \mathbf{u}. \tag{2.5}$$

Taking the curl of (2.5) yields the vorticity equation satisfied by the steady, linear flow:

$$\frac{\partial \mathbf{u}}{\partial z} = -\frac{1}{2} E \nabla^2 \boldsymbol{\omega}, \tag{2.6}$$

where $\boldsymbol{\omega} = \nabla \times \mathbf{u} = \hat{\mathbf{k}} \times \frac{\partial \mathbf{u}_H}{\partial z} - \hat{\mathbf{k}} \times \nabla_H w + \hat{\mathbf{k}}\zeta$ is the relative vorticity and $\zeta = \nabla_H^2 \psi$ is its vertical component. If we assume that the flow varies on a dimensional scale of $O(H_o)$ and expand $\mathbf{u}$ and $\boldsymbol{\omega}$ in powers of the small parameter $E^{\frac{1}{2}}$ (i.e. $\mathbf{u} = \sum_{i=0}^{\infty} E^{\frac{i}{2}} \mathbf{u}_i$ and $\boldsymbol{\omega} = \sum_{i=0}^{\infty} E^{\frac{i}{2}} \boldsymbol{\omega}_i$, with $\mathbf{u}_i$ and $\boldsymbol{\omega}_i$ $O(1)$), the horizontal and vertical components of the vorticity equation yield expressions for the balance between tilting of "planetary" vorticity $2\hat{\mathbf{k}}$ and the viscous diffusion of the resulting horizontal relative vorticity:

$$\frac{\partial \mathbf{u}_{H0}}{\partial z} = \mathbf{0} \tag{2.7}$$

$$\frac{\partial \mathbf{u}_{H1}}{\partial z} = \mathbf{0} \tag{2.8}$$

$$\frac{\partial \mathbf{u}_{H2}}{\partial z} = \frac{1}{2} \nabla_H^2 \left[\hat{\mathbf{k}} \times \nabla_H w_0 \right] \tag{2.9}$$

$$\frac{\partial \mathbf{u}_{H3}}{\partial z} = \frac{1}{2} \nabla_H^2 \left[\hat{\mathbf{k}} \times \nabla_H w_1 \right] \tag{2.10}$$

and the balance between stretching of planetary vorticity and the viscous diffusion of the resulting vertical relative vorticity:

$$\nabla_H \cdot \mathbf{u}_{H0} = -\frac{\partial w_0}{\partial z} = 0 \tag{2.11}$$

$$\nabla_H \cdot \mathbf{u}_{H1} = -\frac{\partial w_1}{\partial z} = 0 \tag{2.12}$$

$$\nabla_H \cdot \mathbf{u}_{H2} = -\frac{\partial w_2}{\partial z} = \frac{1}{2} \nabla_H^2 \zeta_0 \tag{2.13}$$

$$\nabla_H \cdot \mathbf{u}_{H3} = -\frac{\partial w_3}{\partial z} = \frac{1}{2} \nabla_H^2 \zeta_1, \tag{2.14}$$

where we have used the E^0 and $E^{\frac{1}{2}}$ expressions to simplify the $E^{\frac{2}{2}}$ and $E^{\frac{3}{2}}$ expressions, and also used the continuity equation (2.2).

This expansion shows that in a steady, linear flow which varies on a dimensional scale of $O(H_o)$, $\frac{\partial \mathbf{u}_H}{\partial z}$ and $\nabla_H \cdot \mathbf{u}_H$ are at most $O(E)$, even if $\mathbf{u}_H$ and the relative depth variation are $O(1)$. This well-known result (the Taylor-Proudman theorem) is simply a consequence of the flow being geostrophic to $O(E^{\frac{1}{2}})$, as is clear from (2.5). The remainder of this section will investigate the terms at $O(E)$ and $O(E^{\frac{3}{2}})$ in order to obtain more refined estimates of the divergence and depth-dependence of the horizontal flow.

In order to go to higher order we need to determine the magnitudes of w and ζ. In the sliced cone and sliced cylinder the region of interest is bounded above and below by Ekman layers on the upper and lower boundaries. According to steady, linear theory (Greenspan, 1968), to $O(E^{\frac{1}{2}})$ the Ekman pumping velocity due to the upper Ekman layer (on the horizontal lid at $z = 1$) is

$$w_T = \frac{1}{2} E^{\frac{1}{2}} \left(\zeta_T - \zeta \right), \tag{2.15}$$

where $\zeta_T = 2\frac{\epsilon}{|\epsilon|}$ is the vertical component of the vorticity of the lid due to its relative rotation. To $O(E^{\frac{1}{2}})$ the vertical velocity at the stationary bottom boundary at $z = h$ is

$$w_B = \mathbf{u}_H \cdot \nabla_H h + \frac{\sigma}{2} E^{\frac{1}{2}} \left\{ \zeta + s^2 \left(\hat{\mathbf{s}} \times \hat{\mathbf{k}} \right) \cdot \nabla_H (\mathbf{u}_\psi \cdot \hat{\mathbf{s}}) \right\}, \tag{2.16}$$

where $s = |\nabla_H h|$ is the bottom slope, $\hat{\mathbf{s}} = s^{-1} \nabla_H h$ is the unit vector in the direction of increasing h (decreasing depth), and $\sigma = \sqrt[4]{1 + s^2}$. This expression for w_B is derived in Appendix A; it is a coordinate-free form of equation (4.9.32) in Pedlosky (1987*a*) for the case of isotropic viscosity, and is valid where the radius of curvature of the bottom topography is much larger than the Ekman layer thickness. The first term represents orographic uplift of horizontal flow over topography and the second term is the Ekman pumping velocity modified by the bottom slope. For $s \ll 1$ the Ekman layer is essentially the same as that over a flat bottom and the only effect of the slope is to add the orographic term.

From (2.11) and (2.12) we have $w = w_T$ for all z to $O(E^{\frac{1}{2}})$. We also have $w = O(E^{\frac{1}{2}})$ from (2.15), so $w_0 = 0$ and (2.9) immediately yields $\frac{\partial \mathbf{u}_{H2}}{\partial z} = \mathbf{0}$.

Furthermore, since $w_T = w_B$ to $O(E^{\frac{1}{2}})$, we can combine (2.15) and (2.16) to obtain

$$\mathbf{u}_H \cdot \nabla_H h = \frac{1}{2} E^{\frac{1}{2}} \left\{ \zeta_T - (1 + \sigma)\zeta - \sigma s^2 \left(\hat{\mathbf{s}} \times \hat{\mathbf{k}} \right) \cdot \nabla_H (\mathbf{u}_\psi \cdot \hat{\mathbf{s}}) \right\}. \tag{2.17}$$

This expression shows that the orographic term $\mathbf{u}_H \cdot \nabla_H h$ is at most $O(E^{\frac{1}{2}})$, even if $\mathbf{u}_H$ and $\nabla_H h$ are $O(1)$. We will assume from now on that $\nabla_H h \gg E^{\frac{1}{2}}$ (as in the sliced cone and sliced cylinder models used here), which implies that $\mathbf{u}_{H0} \cdot \nabla_H h = 0$, that is, any $O(1)$ flow must be aligned with depth contours. Since $\mathbf{u}_{H0}$ is nondivergent, it can be expressed in terms of a streamfunction $\psi_0 = \psi_0(D)$ which depends only on the fluid depth $D = 1 - h$. Thus the zeroth-order flow is determined by the geometry of the depth contours ("geostrophic contours") and the functional relationship between ψ_0 and D (note however that the function $\psi_0(D)$ may be different in two non-intersecting regions which have the same range of D). The zeroth-order velocity is

$$\mathbf{u}_{H0} = \frac{\mathrm{d}\psi_0}{\mathrm{d}D} \hat{\mathbf{k}} \times \nabla_H D = -s \frac{\mathrm{d}\psi_0}{\mathrm{d}D} \hat{\mathbf{k}} \times \hat{\mathbf{s}}, \tag{2.18}$$

so the zeroth-order velocity on a given depth contour is proportional to the bottom slope s. This expression for $\mathbf{u}_{H0}$ shows that to lowest order the final term vanishes in equation (2.17), which can therefore be written

$$\mathbf{u}_{H1} \cdot \nabla_H h = \frac{1}{2} \left\{ \zeta_T - (1 + \sigma)\zeta_0 \right\}. \tag{2.19}$$

If the flow has a dimensional scale of $O(H_o)$ as we have assumed, a balance of terms in equation (2.19) must involve ζ_T, since it is $O(1)$. We will investigate two limiting cases, in which ζ_T is balanced by only one other term.

If $\mathbf{u}_{H1} \cdot \nabla_H h = 0$, then $\zeta_0 = \frac{\zeta_T}{1+\sigma}$ and (2.15) implies $w_1 = \frac{\sigma}{2(1+\sigma)} \zeta_T$. In regions where ζ_T and σ are spatially uniform (everywhere in the sliced cylinder, and everywhere except the join between the sidewall and the interior in the sliced cone), (2.13) implies $\nabla_H \cdot \mathbf{u}_{H2} = 0$ and (2.10) implies $\frac{\partial \mathbf{u}_{H3}}{\partial z} = \mathbf{0}$.

In the other limit, $\zeta_0 = 0$ and (assuming ζ_T is spatially uniform) we again obtain $\nabla_H \cdot \mathbf{u}_{H2} = 0$ from (2.13) and $\frac{\partial \mathbf{u}_{H3}}{\partial z} = \mathbf{0}$ from (2.15) and (2.10). This second limit (in

which the flow is driven across depth contours by the vorticity input by the lid) will be referred to as a topographic Sverdrup balance. It is analogous to the Sverdrup (1947) balance on a β-plane, in which the surface wind stress drives a meridional flow.

Using (2.5), (2.7) and (2.11), the steady, linear horizontal momentum equation at $O(E)$ can be written

$$2\hat{\mathbf{k}} \times \mathbf{u}_{H2} = -\nabla p_2 + \hat{\mathbf{k}} \times \nabla_H \zeta_0. \tag{2.20}$$

Since $\nabla_H \zeta_0 = \mathbf{0}$ in both limits above, it is clear that the steady, linear flow is geostrophic to $O(E)$ in these limits.

These limits may appear artificial, but it is easy to show that they apply to most of the flow in the sliced cone and sliced cylinder.

In the sliced cylinder, every depth contour intersects the sidewall (i.e. this geometry is "geostrophically blocked"), so we must have $\psi_0 = 0$ in order to match ψ_0 with its value at the boundary. We therefore have $\zeta_0 = 0$, so the topographic Sverdrup balance is obtained everywhere in the sliced cylinder where the flow has a dimensional scale of $O(H_o)$; this was first demonstrated by Pedlosky & Greenspan (1967). The return flow takes place in a western boundary current which is much narrower than this length scale, so that $|\zeta| \gg |\zeta_T|$ and a different vorticity balance therefore occurs (this is discussed in the following section).

The situation in the sliced cone is a little more subtle, since every depth contour is a closed curve (i.e. this geometry is "geostrophically guided"). Using the relationship between the zeroth-order streamfunction and the depth, the zeroth-order vorticity is

$$\zeta_0 = \nabla_H^2 \psi_0 = s^2 \frac{\mathrm{d}^2 \psi_0}{\mathrm{d}D^2} + \frac{\mathrm{d}\psi_0}{\mathrm{d}D} \nabla_H^2 D, \tag{2.21}$$

where the first term on the right-hand side is the vorticity due to the cross-isobath shear in the velocity, and the second term is the vorticity due to flow along curved or unequally spaced depth contours. In the planar sloping interior of the sliced cone ($r < r_e$) we have $\nabla_H^2 D = 0$ and $s^2 = 10^{-2}$. Since $\mathrm{d}^2\psi_0/\mathrm{d}D^2$ is at most $O(1)$ (and is found from numerical experiments to actually be much smaller), we have $|\zeta_0| \ll |\zeta_T|$ in this region, and therefore an approximate topographic Sverdrup balance. On the upper part of the slope, where $r > r_{e_{max}}$ and so depth contours do not cross into the interior, we have $\frac{\partial D}{\partial \theta} = 0$, where θ is the azimuthal coordinate. Therefore from (2.21) we have $\frac{\partial \zeta_0}{\partial \theta} = 0$ and so (2.19) implies $\frac{\partial}{\partial \theta}(\mathbf{u}_{H1} \cdot \nabla_H h) = 0$, since ζ_T and σ are spatially uniform in this region. By using this result and applying Gauss' theorem to the integral of $\nabla_H \cdot \mathbf{u}_{H1}$ over the area bounded by each depth contour in this region it is evident that since $\nabla_H \cdot \mathbf{u}_{H1} = 0$ from (2.12) we must have $\mathbf{u}_{H1} \cdot \nabla_H h = 0$ throughout the region $r > r_{e_{max}}$, which corresponds to the first limit discussed above. The vorticity balances in these regions are the same as those predicted by the linear theory of Griffiths & Veronis (1998). The balance in the remaining region (the lower part of the slope, $r_e < r < r_{e_{max}}$, where depth contours cross the interior) is more complex, due to a cross-contour flow which balances the Sverdrup flow in the interior. Equation (2.19) does not reduce to either limit in this region, since the vorticity is neither spatially uniform nor small; from equation (2.18) we expect the azimuthal velocity in this region to be about an order of magnitude larger than the zonal velocity on the same depth contours in the interior.

To summarise, it has been shown that in regions where the flow varies on a dimensional scale of $O(H_o)$ there is a topographic Sverdrup balance in the sliced cylinder and the interior of the sliced cone, and a balance between (spatially uniform) upper and lower Ekman-layer pumping on the upper part of the slope in the sliced cone. These balances

imply that the horizontal velocity is depth-independent to $O(E^{\frac{3}{2}})$ and horizontally nondivergent to $O(E)$ in these regions. These balances are not obtained on the lower part of the slope in the sliced cone and the horizontal velocity is therefore depth-independent to $O(E)$ and horizontally nondivergent to $O(E^{\frac{1}{2}})$. Since the horizontal velocity is only weakly divergent, it can be well represented by a streamfunction.

It is illuminating to compare the very small divergence and depth dependence in this system with flow over topography when the Coriolis force is spatially variable (i.e. $\beta \neq 0$). Although β is equivalent to $s = |\nabla_{H} h|$ in terms of the ambient potential vorticity gradient in the quasigeostrophic limit $h \ll 1$, β has a direct effect on the horizontal divergence of the flow outside the Ekman layers, whereas the depth gradient is "felt" only through the vertical stretching, which is very restricted when $\beta = 0$. To see this, we replace $2\hat{\mathbf{k}}\times\mathbf{u}$ with $2(1+\beta y)\hat{\mathbf{k}}\times\mathbf{u}$ in (2.5) and take the curl as before. To $O(E^{\frac{3}{2}})$ the horizontal component of the resulting vorticity equation is

$$\frac{\partial \mathbf{u}_{H}}{\partial z} = \frac{E}{2(1+\beta y)} \nabla_{H}^{2} \left[\hat{\mathbf{k}} \times \nabla_{H} w \right], \tag{2.22}$$

so the depth-independence of the *horizontal* velocity is basically unaltered from that predicted by (2.7)–(2.10). In contrast, the vertical component of the vorticity equation becomes

$$\nabla_{H} \cdot \mathbf{u}_{H} = -\frac{\partial w}{\partial z} = \frac{E}{2(1+\beta y)} \nabla_{H}^{2} \zeta - \frac{\beta v}{1+\beta y}, \tag{2.23}$$

so the magnitude of $\frac{\partial w}{\partial z}$ (and hence $\nabla_{H} \cdot \mathbf{u}_{H}$) is fundamentally changed from that given by (2.11)–(2.14), since the additional β term can balance a much greater horizontal divergence than the horizontal viscosity alone could support.

An application of the continuity equation to (2.22) shows that $\frac{\partial^2 w}{\partial z^2} = 0$ to $O(E^{\frac{1}{2}})$, so $\frac{\partial w}{\partial z} = D^{-1}(w_{T} - w_{B})$ to $O(E^{\frac{1}{2}})$ as before. However equation (2.23) shows that the upper and lower vertical velocities w_{T} and w_{B} can differ by up to $O(\beta)$, so the cross-isobath component of the velocity is much less restricted than in the case of zero β, where w_{T} and w_{B} can differ by at most $O(E)$. In order for the orographic and β terms to balance, large-scale $O(1)$ flow must be aligned with contours of $(1+\beta y)/D$ rather than D. An $O(1)$ flow along $(1+\beta y)/D$ contours which are significantly inclined to the depth contours—for example over a western boundary slope of $O(\beta)$—can result in a horizontal divergence of up to $O(\beta)$. In this situation there is no question of using a streamfunction to accurately represent the horizontal velocity. A *transport* streamfunction can be used (as in Becker, 1999; Becker & Salmon, 1997; Holland, 1967), but this must either include the Ekman layer transport or neglect the $O(E^{\frac{1}{2}})$ transport divergence in the interior due to Ekman pumping.

The horizontal divergence of the horizontal velocity is smaller when β *replaces* the depth gradient than when both are present, but it is still larger than in the case of topography alone. For example, the horizontal divergence of Sverdrup flow on a β-plane exceeds that of the analogous topographic Sverdrup flow by a factor of $O(E^{-\frac{1}{2}})$, because w_{B} does not match the Ekman pumping velocity w_{T}.

2.2.2 Linear theory of sidewall boundary layers in the sliced cylinder

It was shown in the previous section that in the linear limit the large-scale flow in the sliced cylinder is in a Sverdrup balance to $O(E^{\frac{1}{2}})$, with the velocity component normal to depth contours given by $v_{Sv} = E^{\frac{1}{2}}\zeta_{T}/(2s)$. To this order the along-contour velocity component

can be determined by horizontal nondivergence and the condition of no normal flow at the eastern boundary ($-\pi/2 < \theta < \pi/2$), giving the interior Sverdrup streamfunction

$$\psi_{Sv} = v_{Sv}[x - (\Lambda^2 - y^2)^{\frac{1}{2}}] \tag{2.24}$$

derived by Pedlosky & Greenspan (1967). It is immediately apparent that the Sverdrup streamfunction satisfies neither the condition of no normal flow at the western boundary, nor the no-slip condition. This section will discuss the boundary layers (with length scale much smaller than that considered in the previous section) which arise in order to satisfy these boundary conditions, and also to close the secondary vertical circulation. Apart from the estimates of the depth-dependence and horizontal divergence of $\mathbf{u}_H$, the analysis and discussion presented in this section is largely due to Beardsley (1969). It is included in order to introduce terminology and equations for later use and to investigate the extent to which flow on smaller scales remains horizontally nondivergent and depth independent. In addition the results for the sliced cylinder have important consequences for the boundary current at the west of the interior in the sliced cone.

We begin by investigating the boundary layers required to satisfy the lateral boundary conditions and close the horizontal circulation. If we assume that the horizontal velocity is independent of depth to lowest order, the continuity equation (2.2) implies that the vertical velocity w is a linear function of depth, so the stretching term $\frac{\partial w}{\partial z}$ can be determined from the values w_T and w_B given by (2.15) and (2.16), assuming that the lateral boundary layer thickness is much greater than $E^{\frac{1}{2}}$. The vertical component of the steady linear vorticity equation (2.6) then becomes

$$(1-h)^{-1}[2\mathbf{u}_H \cdot \nabla_H h - E^{\frac{1}{2}}(\zeta_T - 2\zeta)] = E\nabla_H^2 \zeta, \tag{2.25}$$

where we have neglected the slope correction to the bottom Ekman friction in (2.16).

The viscous boundary layers in the sliced cylinder can be understood most easily by considering the flow near the western boundary at $\theta = \pi$, where $h = sy = 0$. Making the boundary layer approximation $\frac{\partial}{\partial x} \gg \frac{\partial}{\partial y}$, we neglect derivatives in the y direction (including the curvature of the boundary) so the vorticity equation (2.25) at $\theta = \pi$ becomes

$$E\frac{\mathrm{d}^3 v}{\mathrm{d}X^3} - 2E^{\frac{1}{2}}\frac{\mathrm{d}v}{\mathrm{d}X} - 2sv = -E^{\frac{1}{2}}\zeta_T, \tag{2.26}$$

where $X = x + \Lambda$ is the x coordinate with its origin at the western boundary and v is the northward velocity. We seek solutions to this ordinary differential equation subject to the conditions $v(X = 0) = 0$ (no-slip at the west), $v(X \gg 0) \to v_{Sv} = E^{\frac{1}{2}}\zeta_T/(2s)$ (v matches the Sverdrup velocity far from the western boundary), and $\int_0^{2\Lambda} v(X)\,\mathrm{d}X = 0$ (conservation of volume[2]).

The particular solution of this ordinary differential equation is the Sverdrup solution $v = v_{Sv}$. The complete solution is of the form $v = v_{Sv} + \sum_{n=1}^{3} C_n \exp(\lambda_n X)$, where the λ_n are the three roots of the characteristic polynomial

$$\lambda^3 - 2E^{-\frac{1}{2}}\lambda - 2sE^{-1} = 0. \tag{2.27}$$

One of these roots (which we will denote λ_1) is always real and positive, regardless of the values of E and $s > 0$; we must therefore have $C_1 = 0$ in order to match the Sverdrup solution in the east (this root corresponds to the Stewartson $E^{\frac{1}{4}}$ layer at the eastern

[2]The Stewartson $E^{\frac{1}{4}}$ layer at the eastern boundary makes an insignificant contribution to the transport and has been neglected.

boundary which brings the azimuthal Sverdrup velocity to zero to satisfy the no-slip boundary condition).

The nature of the remaining two roots depends on the size of s relative to $s_{cr} = (2/3)^{\frac{3}{2}} E^{\frac{1}{4}}$. For $s \leq s_{cr}$ the roots are real and negative, and represent boundary layers which decay monotonically with distance from the western boundary. In the limit $s \ll s_{cr}$ these roots are widely separated. The less negative root $\lambda_2 = -sE^{-\frac{1}{2}}$ corresponds to a layer of thickness $\delta_S = s^{-1}E^{\frac{1}{2}}$ in which the vorticity balance is between orographic vortex stretching and suction through the top and bottom Ekman layers due to the relative vorticity of the flow (the last two terms on the left hand side of (2.26)). This layer is the topographic analogue of the Stommel (1948) western boundary current on a β-plane; this layer returns the Sverdrup transport of $O(2\Lambda E^{\frac{1}{2}}/s)$, and therefore has an azimuthal velocity of $O(2\Lambda)$. Embedded within the Stommel layer is a thin Stewartson $E^{\frac{1}{4}}$ sublayer against the boundary (Stewartson, 1957), where the azimuthal velocity is brought to zero through a balance between lateral viscosity and Ekman friction (the first two terms on the left hand side of (2.26)); this layer corresponds to the more negative root $\lambda_3 = -2^{\frac{1}{2}}E^{-\frac{1}{4}}$.

As the bottom slope s increases towards $E^{\frac{1}{4}}$, the Stommel boundary current thickness and transport decrease towards values characteristic of a Stewartson $E^{\frac{1}{4}}$ layer, whilst the Stewartson layer thickens slightly. When $s \sim E^{\frac{1}{4}}$ lateral viscosity is significant in the Stommel layer, and the orographic term is comparable to Ekman suction in balancing the lateral diffusion of vorticity through the boundary in the Stewartson $E^{\frac{1}{4}}$ layer; in the sliced cylinder this orographic modification to the Stewartson $E^{\frac{1}{4}}$ layer is strongest at the west ($\theta \approx \pi$), where the azimuthal velocity is parallel to the depth gradient.

When $s = s_{cr} = (2/3)^{\frac{3}{2}} E^{\frac{1}{4}}$ the Stommel boundary current merges with the modified Stewartson $E^{\frac{1}{4}}$ layer at $\theta = \pi$, and $\lambda_2 = \lambda_3 = -(2/3)^{\frac{1}{2}}E^{-\frac{1}{4}}$. When s increases beyond s_{cr} the two roots form the complex conjugate pair $\lambda_2 = \lambda_3^* = \lambda_r + i\lambda_i$, with $\lambda_r < 0$, and the solution satisfying the boundary conditions is

$$v = v_{Sv} - v_{Sv} e^{\lambda_r X} \left\{ \cos \lambda_i X + \lambda_i^{-1} [2\Lambda(\lambda_r^2 + \lambda_i^2) + \lambda_r] \sin \lambda_i X \right\}, \tag{2.28}$$

where we have assumed $|\lambda_r^{-1}| \ll 2\Lambda$, i.e. the boundary layer is much thinner than the basin width. Thus when $s > s_{cr}$ the two monotonically decaying boundary layers are replaced by a single boundary current with an oscillatory decay in X, which returns the interior Sverdrup transport through $y = 0$ and also satisfies the no-slip boundary condition at $X = 0$. All three terms on the left hand side of (2.26) are important in this combined western boundary current when $s \approx s_{cr}$. The meridional extent of the combined boundary layer increases rapidly with s beyond this critical value, and it occupies the entire western boundary $\pi/2 \leq \theta \leq 3\pi/2$ in the limit $s \gg s_{cr}$ (Beardsley, 1969). In this limit we have $\lambda_r = -(\frac{s}{4E})^{\frac{1}{3}} \equiv -\delta_M^{-1}$ and $\lambda_i = -3^{\frac{1}{2}}\lambda_r$, and the western boundary current vorticity balance is entirely between orographic vortex stretching and lateral viscosity (the first and third terms on the left hand side of (2.26)). This limit is analogous to the Munk (1950) model of western boundary currents on a β-plane; the thickness scale of the western boundary current is $\delta_M = (4E/s)^{\frac{1}{3}}$, and the velocity in the western boundary current scales as $\Lambda E^{\frac{1}{6}} s^{-\frac{2}{3}}$ (by continuity).

We can estimate the magnitude of the divergent component $\nabla_H \phi$ of the horizontal velocity by using the continuity equation and the vertical component of the vorticity equation (2.6): $\nabla_H \phi \sim \delta \frac{\partial w}{\partial z} \sim \delta E \nabla_H^2 \zeta \sim \delta^{-2} E v$, where δ and v are the length and (nondivergent) velocity scales of the flow. In the limit $s \ll E^{\frac{1}{4}}$ this gives $\nabla_H \phi \sim \Lambda s^2$ in the Stommel layer and $\nabla_H \phi \sim \Lambda E^{\frac{1}{2}}$ in the Stewartson $E^{\frac{1}{4}}$ viscous sublayer, both very much less than the horizontally nondivergent velocity, $\hat{\mathbf{k}} \times \nabla_H \psi \sim \Lambda$. The divergent velocity in the

Stommel layer increases as the bottom slope increases, until $\nabla_H \phi \sim \Lambda E^{\frac{1}{2}}$ when $s = O(E^{\frac{1}{4}})$. Further increase in the bottom slope does not increase the divergent component of the velocity, but does reduce the nondivergent component. In the Munk limit $s \gg E^{\frac{1}{4}}$ we have $\nabla_H \phi \sim \Lambda E^{\frac{1}{2}}$ and $\hat{\mathbf{k}} \times \nabla_H \psi \sim \Lambda E^{\frac{1}{6}} s^{-\frac{2}{3}}$ away from the no-slip western boundary; the divergent velocity becomes comparable to the maximum nondivergent velocity when $s = O(E^{-\frac{1}{2}})$. For comparison, the divergence of the Stommel boundary current on the analogous β-plane is much larger ($\nabla_H \phi \sim \Lambda E^{\frac{1}{2}}$) because there is no orographic vortex compression to cancel the stretching due to Ekman suction. The Munk layer is less divergent on the β-plane because stretching is not involved in the primary vorticity balance; thus $\nabla_H \phi \sim \Lambda E^{\frac{2}{3}} \beta^{-\frac{2}{3}}$ due to Ekman suction.

The depth-dependence of the horizontal velocity in the western boundary current can be estimated in a similar way. The leading terms of the horizontal components of the vorticity equation (2.6) yield $\frac{\partial \mathbf{u}_H}{\partial z} \approx \frac{E}{2} \nabla_H^2 \left[\hat{\mathbf{k}} \times \nabla_H w \right]$. Since $w \sim w_B \sim sv[1 \pm \delta_S/(2\delta)]$ from (2.16), we have $\frac{1}{v}\frac{\partial v}{\partial z} \sim E\delta^{-3} s[1 \pm \delta_S/(2\delta)]$, where δ is the width of the boundary layer under consideration. In the limit $s \ll E^{\frac{1}{4}}$ this gives $\frac{1}{v}\frac{\partial v}{\partial z} \sim E^{-\frac{1}{2}} s^4 \ll E^{\frac{1}{2}}$ in the Stommel layer ($\delta = \delta_S$) and $\frac{1}{v}\frac{\partial v}{\partial z} \sim E^{\frac{1}{2}}$ in the viscous sublayer, where $\delta = E^{\frac{1}{4}} 2^{-\frac{1}{2}} \ll \delta_S$. In the Munk limit $s \gg E^{\frac{1}{4}}$ we have $\delta = \delta_M \gg \delta_S$, giving $\frac{1}{v}\frac{\partial v}{\partial z} \sim s^2$. For $E \approx 10^{-4}$ and $s \approx 0.1$ as in the experimental regime considered here, all three estimates predict that v is independent of depth to within about one percent (this confirms the self-consistency of assuming depth-independent flow in deriving (2.25)).

We now come to the question of closing the vertical circulation. Under anticyclonic forcing there is a horizontally convergent flow directed radially inwards in the upper Ekman layer, which therefore pumps fluid downwards into the interior (the flow is in the opposite direction under cyclonic forcing). This fluid is supplied by an upwelling flow within a Stewartson layer of thickness $E^{\frac{1}{3}}$ embedded within the Stewartson $E^{\frac{1}{4}}$ layer at the sidewall (Stewartson, 1957). The flow in this layer is non-hydrostatic (the vertical momentum balance is between lateral viscosity and a vertical pressure gradient), and the horizontal velocity is strongly depth-dependent (Friedlander, 1980; Greenspan, 1968). Since the horizontal basin integral of the vertical vorticity ζ is zero as a consequence of Green's theorem and the no-slip boundary condition, the basin-integrated flux into the bottom Ekman layer also vanishes if we neglect the finite-slope corrections (this is discussed in more detail in section 2.3.3). Thus the Stewartson $E^{\frac{1}{3}}$ layer must obtain nearly all the return flux directly from the interior via a radial flow near the boundary.

We will see later that the vorticity balances on the lower part of the slope ($r_e < r < r_{e_{max}}$) and western interior of the sliced cone are similar to those in the sliced cylinder western boundary layers discussed above. In fact for $\theta \approx \pi$ the western boundary current in the interior of the sliced cone is governed by the same differential equation (2.26) as in the sliced cylinder, except that the boundary conditions are different and $X = x + r_e(\theta = \pi)$. The general solution is of the same form, but with different coefficients C_n. In particular the λ_n are determined by (2.27) as before, so the nature of these roots depends on the size of the interior slope s_i relative to s_{cr}. Thus when $s_i < s_{cr}$ there can exist a Stommel layer with a Stewartson $E^{\frac{1}{4}}$ sublayer, which are both monotonic in X; when $s_i > s_{cr}$ these layers must merge into a single boundary layer which is oscillatory in X.

2.3 Governing equations for the numerical model

We will now return to the full momentum equation (2.1) and use the results obtained in sections 2.2.1 and 2.2.2 to derive a simplified equation governing the evolution of the horizontal flow in the sliced cone and sliced cylinder at nonzero Rossby number. This task is made more difficult by the $O(1)$ depth variation in the sliced cone, which precludes the use of the standard quasigeostrophic approximation. Previous numerical studies of flow in this situation (Becker, 1995, 1999; Becker & Salmon, 1997; Holland, 1967) used the depth-integrated momentum equation and expressed the flow in terms of a transport streamfunction. This approach involves integrating through the entire vertical extent of the flow, including the Ekman layers, so the transport streamfunction includes a contribution from the Ekman transport. I have followed a different approach because I am concerned with the flow in the bulk of the fluid (outside the Ekman layers), since this is what was measured in the laboratory.

It was shown in sections 2.2.1 and 2.2.2 that in the sliced cone and sliced cylinder the horizontal velocity outside the Ekman layers and sidewall Stewartson $E^{\frac{1}{3}}$ layers is very nearly depth-independent and horizontally nondivergent, despite large variations in depth. We begin by investigating the consequences of depth-independence. We expect that the horizontal velocity will retain its depth-independence when advection and time-dependence are relatively weak, since the limit $Ro \to 0$ is not singular; this was confirmed experimentally by GV97 for all Rossby numbers investigated. We will therefore assume that $\frac{\partial \mathbf{u}_H}{\partial z} = \mathbf{0}$ outside the Ekman layers, which allows the horizontal flow in this region to be determined at all depths if it can be calculated at one particular depth. Thus we will derive an evolution equation for the horizontal velocity in a thin horizontal sheet just below the top Ekman layer, which will then give the horizontal velocity at all lower depths until the bottom Ekman layer is reached. By assuming that $\frac{\partial \mathbf{u}_H}{\partial z} = \mathbf{0}$ we will not be able to capture the dynamics of the Stewartson $E^{\frac{1}{3}}$ sidewall layer, but its omission will have only a minor effect on the interior flow since it acts only to passively absorb any net horizontal divergence.

With this assumption of depth-independence, the relative vorticity takes the form

$$\boldsymbol{\omega} = \nabla \times \mathbf{u} = (\nabla_H w) \times \hat{\mathbf{k}} + \zeta \hat{\mathbf{k}}, \tag{2.29}$$

and the vertical component of the curl of equation (2.1) yields the vorticity equation

$$Ro \left[\frac{\partial \zeta}{\partial t} + \nabla_H \cdot (\mathbf{u}_H \zeta) \right] - 2 \frac{\partial w}{\partial z} = E \nabla_H^2 \zeta. \tag{2.30}$$

Note that the tilting term $Ro[(\nabla_H w) \times \hat{\mathbf{k}}] \cdot \nabla_H w$ is identically zero, regardless of the size of w and $\nabla_H w$. Thus the horizontal component of the relative vorticity does not appear in equation (2.30) as a consequence of the assumption that $\frac{\partial \mathbf{u}_H}{\partial z} = \mathbf{0}$.

The continuity equation (2.2) implies that the vertical velocity w is a linear function of depth in a region where $\frac{\partial \mathbf{u}_H}{\partial z} = \mathbf{0}$, so the stretching term $\frac{\partial w}{\partial z}$ can be determined from the values w_T and w_B of w at the top and bottom of this region. In our case the steady, linear[3] Ekman matching conditions (2.15) and (2.16) can be used to obtain w_T and w_B,

[3]Steady Ekman matching conditions are valid for flows which are nearly steady over one rotation period (Beardsley, 1975), which is the case here. The use of linear Ekman theory in a flow with Stewartson $E^{\frac{1}{4}}$ layers requires $Ro \ll E^{\frac{1}{4}}$ (Bennetts & Hocking, 1973); this criterion is violated for the more strongly forced results presented here, but linear theory was used because a simple analytic expression for Ekman pumping is only available in the linear limit. The close agreement between the numerical and laboratory results suggests that the error involved is insignificant.

yielding

$$\frac{\partial w}{\partial z} = \frac{w_{_T} - w_{_B}}{D} = \mathbf{u}_{_H} \cdot \nabla_{_H} \ln D + \mathfrak{E}, \tag{2.31}$$

where $D = 1 - h$ is the scaled fluid depth,

$$\mathfrak{E} = \frac{E^{\frac{1}{2}}}{2D} \left[\zeta_{_T} - (1+\sigma)\zeta - \sigma s^2 \left(\hat{\mathbf{s}} \times \hat{\mathbf{k}} \right) \cdot \nabla_{_H} (\mathbf{u}_{_\psi} \cdot \hat{\mathbf{s}}) \right] \tag{2.32}$$

is the stretching due to Ekman pumping, and in the orographic term I have used the identity $(1-h)^{-1}\nabla_{_H} h = -\nabla_{_H} \ln D$. Equation (2.30) is analogous to the shallow-water vorticity equation in oceanographic theory (Pedlosky, 1987*a*), which also requires $\frac{\partial \mathbf{u}_{_H}}{\partial z} = \mathbf{0}$. In the oceanographic case this results from the shallowness of the oceans in relation to their breadth, but such restrictions are not required in the laboratory since depth-independence follows from the effects of rotation alone.

So far we have assumed only that the horizontal velocity is independent of depth. However we found from the analysis in sections 2.2.1 and 2.2.2 that the steady, linear horizontal flow is dominated by its nondivergent component $\mathbf{u}_{_\psi}$, even if $\mathbf{u}_{_H}$ and $\nabla_{_H} \ln D$ are $O(1)$. We expect that the horizontal divergence remains small for moderate Ro (this is confirmed even for strongly nonlinear, time-dependent flow in sections 3.7 and 4.7), so the horizontal velocity is dominated by the nondivergent component in the advection term of the vorticity equation (2.30), and in the orographic component of the stretching term (2.31). To take advantage of this in simplifying the vorticity equation we relax the continuity equation (2.2) and consider the term $\frac{\partial w}{\partial z}$ in equation (2.30) purely as a source of *vorticity*, ignoring its equivalence to the divergence of the *velocity* $-\nabla_{_H} \cdot \mathbf{u}_{_H}$; thus the vorticity production is included without regard to the mechanism (vortex stretching) by which it is generated. Following this approach, the small divergent component of the horizontal velocity in the advection and orographic terms of equations (2.30) and (2.31) will be neglected, yielding the approximate vorticity equation

$$Ro \left[\frac{\partial \zeta}{\partial t} + \nabla_{_H} \cdot \left(\mathbf{u}_{_\psi} \zeta \right) \right] = 2\nabla_{_H} \cdot \left(\mathbf{u}_{_\psi} \ln D \right) + 2\mathfrak{E} + E\nabla_{_H}^2 \zeta \tag{2.33}$$

which together with the Poisson equation

$$\zeta = \nabla_{_H}^2 \psi \tag{2.34}$$

forms a closed system for the evaluation of the nondivergent component $\mathbf{u}_{_\psi} = \hat{\mathbf{k}} \times \nabla_{_H} \psi$ of the horizontal velocity. These equations form the basis of the numerical model. Note that the assumption of horizontal nondivergence has also allowed the orographic term in (2.33) to be written as a divergence, highlighting the important conservation properties of this formulation which will be discussed shortly.

Since (by the continuity equation) $\nabla_{_H} \cdot (\mathbf{u}_{_H} \zeta) = \nabla_{_H} \cdot (\mathbf{u}_{_\psi} \zeta) + \nabla_{_H} \phi \cdot \nabla_{_H} \zeta - \zeta \frac{\partial w}{\partial z}$, by neglecting the horizontally divergent velocity in the advection term we have actually neglected vorticity production by the stretching of ζ, and only the stretching of "planetary" vorticity is retained; this limits the validity of equation (2.33) to $Ro|\zeta| \ll 2$ *in regions where there is stretching.* Although it is a simple matter to include the stretching of ζ (as in Matsuura & Yamagata, 1986; Page, 1981, 1982), this was avoided because firstly it is ad hoc to include this term while neglecting the advection of ζ by $\nabla_{_H} \phi$, and secondly, when the stretching of ζ is neglected we obtain a vorticity equation which conserves the kinetic energy K in the limit $E \to 0$ (see section 2.3.3).

Even though it is valid for flows with $O(1)$ topography, equation (2.33) is nearly identical to the quasigeostrophic vorticity equation obtained by Beardsley (1972), the only differences being the inclusion of the variation of D in the denominator of $\frac{\partial w}{\partial z}$, and the finite-slope correction to the Ekman pumping. Beardsley (1972) followed Greenspan (1969) in using a perturbation expansion in the bottom slope, and therefore obtained a vorticity equation which is valid only for small relative depth variations. The derivation by Greenspan (1969) was intended to demonstrate the analogy between β and the depth gradient, rather than produce a vorticity equation which models the laboratory flow with great accuracy; this analogy holds only for small relative depth variations, so these were the conditions under which the equation was derived. Subsequent authors (e.g. Beardsley & Robbins, 1975) have generally followed a similar approach, creating an impression that the validity of a vorticity equation of this form to laboratory flows is limited to the conditions used by Greenspan[4]. However it is the depth-independence and horizontal nondivergence of the horizontal velocity implied by these conditions which are responsible for the form of the vorticity equation. The derivation presented here shows that provided the horizontal velocity is nearly nondivergent, only very minor modifications are needed to make Beardsley's vorticity equation applicable to a much wider range of conditions (depth variations of $O(1)$), a generality that appears not to have been previously recognised.

There are many "intermediate models" (Allen *et al.*, 1990; McWilliams & Gent, 1980) which also seek, among other things, to generalise quasigeostrophic theory to allow $O(1)$ variations in topography. Such models typically have undesirable mathematical properties, such as non-conservation of potential vorticity and/or energy (Allen *et al.*, 1990), due to the inclusion of some higher-order effects of the horizontal velocity divergence (e.g. in the advection term). By virtue of the near-nondivergence of the horizontal flow in our case due to the absence of β and stratification and the restriction to small Rossby number, we have obtained a formulation which describes the flow over large-amplitude topography while retaining the simplicity of quasigeostrophic theory. We will see below that this formulation also retains important conservation properties of the quasigeostrophic vorticity equation. The accuracy of this approach will be demonstrated in Chapters 3 and 4.

2.3.1 Potential vorticity

As a consequence of neglecting the stretching of relative vorticity, equation (2.33) does *not* conserve the shallow-water potential vorticity $q = \frac{Ro\zeta+2}{D}$ in the limit of vanishing E (as (2.30) does), but rather the related quantity

$$Q = Ro\zeta - 2\ln D, \tag{2.35}$$

which reduces to the quasigeostrophic potential vorticity $Ro\zeta + 2h$ for $|h| \ll 1$. It is more convenient to express Q as an "effective depth"

$$D_{\mathit{eff}} = e^{-Q/2} = De^{-Ro\zeta/2}, \tag{2.36}$$

since this avoids the singularity in Q at the boundary of the sliced cone where the depth vanishes. In addition, D_{eff} reduces to the actual depth in the linear limit and allows us to generalise the intuition obtained for steady, linear flow to the transient nonlinear case

[4]Beardsley (1973) presented an alternative derivation which avoided a perturbation expansion in the bottom slope, but still concluded that the slope needed to be vanishingly small, since he seems not to have recognized that finite depth variations can be included if we identify β with the gradient of the *logarithm* of D.

(note that the gradient of D_{eff} is antiparallel to the gradient of the potential vorticity Q). Using D_{eff}, the vorticity equation (2.33) can be written

$$\frac{\partial D_{\mathit{eff}}}{\partial t} + \nabla_H \cdot \left(\mathbf{u}_\psi D_{\mathit{eff}}\right) = \frac{-D_{\mathit{eff}}}{2}\left[2\mathfrak{E} + E\nabla_H^2\zeta\right], \tag{2.37}$$

showing that in the absence of dissipation each fluid parcel must conserve its value of D_{eff}. Note that dissipation is less effective where D_{eff} is small (e.g. near $r = \Lambda$ in the sliced cone), so streamlines become very closely aligned with D_{eff} contours in these regions. The restriction $Ro|\zeta| \ll 2$ required for the stretching of relative vorticity to be negligible implies that $e^{-1} \ll D_{\mathit{eff}}/D \ll e$—that is, the formulation is not accurate when the effective depth is very different from the actual depth.

2.3.2 Boundary conditions

Recall that the approach taken here is to derive equations for the uppermost horizontal layer, and to assume that the calculated horizontal flow applies to the full depth of the fluid outside the Ekman layers. Note that the lateral boundary of a deeper layer is not necessarily at $r = \Lambda$, but may instead be at the geostrophic contour corresponding to the depth of the layer (for example the contours shown in figure 2.1 (b) for the sliced cone). When the boundary of a layer is not at $r = \Lambda$, the boundary conditions are determined by the *interior* flow in shallower layers, rather than specified in the formulation of the problem; thus (for example) there can be "inflow" and "outflow" across the boundary of each lower layer in the sliced cone[5]. Only at $r = \Lambda$ must the lateral boundary conditions be specified in advance, since there is no interior flow at shallower depth. Although only the infinitesimally thin uppermost layer is exposed to the boundary conditions at $r = \Lambda$ in the sliced cone, they are nevertheless important because the effect they have on the flow in this layer will implicitly determine the lateral boundary conditions for the flow in lower layers.

The kinematic condition of no normal flow was imposed on the lateral boundary of the uppermost layer in both the sliced cone and sliced cylinder:

$$\psi = 0 \qquad \text{at} \quad r = \Lambda. \tag{2.38}$$

This condition is consistent with the formulation, since it is not possible to have a net horizontal flux through the boundary when the horizontal divergence of the flow is neglected. Thus this formulation cannot include any net radial flux into the Stewartson $E^{\frac{1}{3}}$ sidewall layer in the sliced cylinder.

A higher-order boundary condition is also required. The no-slip boundary condition

$$\frac{\partial \psi}{\partial r} = 0 \qquad \text{at} \quad r = \Lambda \tag{2.39}$$

is satisfied in the sliced cylinder by boundary layers in which the flow is depth-independent and horizontally nondivergent to lowest order, as discussed in section 2.2.2. These boundary layers are therefore captured by this formulation, so this boundary condition is appropriate for the sliced cylinder and was used for almost all the numerical runs. Numerous studies (Blandford, 1971; Chassignet & Gent, 1991; Dengg, 1993; Haidvogel *et al.*, 1992; Verron & Blayo, 1996) have demonstrated that the nature of nonlinear wind-driven flow

[5]There can be no *net* "inflow" or "outflow" due to the assumption of horizontal nondivergence. Of course these "inflows" and "outflows" actually pass out of or into shallower layers rather than through the sloping sidewall, because $\mathbf{u} = \mathbf{u}_H + \hat{\mathbf{k}}w$ is parallel to the bottom boundary.

in ocean models is critically dependent on the boundary conditions used and their implementation. In order to test the sensitivity of the sliced cylinder results to the choice of boundary conditions a few runs were also conducted with the free-slip condition

$$\zeta = 0 \qquad \text{at} \quad r = \Lambda. \tag{2.40}$$

The results of these free-slip experiments are reported in section 5.3.

The choice of the higher-order boundary condition in the sliced cone is less clear-cut. Many numerical runs were conducted with the no-slip condition (2.39), but its appropriateness to the interior flow in this geometry is questionable since the lateral boundary is "buried" beneath the merged upper and lower Ekman layers. On the upper slope GV97 saw no radial flow outside the Ekman layers, but observed a vertical recirculation of dye from the interior through the two Ekman layers and back to the interior at the same radius. This indicates that the direct connection between the upper and lower Ekman layers removes the need for horizontal flow into a Stewartson $E^{\frac{1}{3}}$ layer at the lateral boundary of the sliced cone. It is questionable whether the observed mechanism for returning fluid pumped into the interior to the upper Ekman layer could function if the flow outside the Ekman layers were subject to the no-slip condition, since its basin-integrated vorticity would vanish (see section 2.3.3), so the net vertical flux out of the bottom Ekman layer would also vanish if not for the finite-slope corrections in equation (2.16).

A few sliced cone runs were conducted with the free-slip boundary condition (2.40), but a more appropriate boundary condition (also used for a few runs) is probably

$$\zeta = \frac{\zeta_T}{1+\sigma} \qquad \text{at} \quad r = \Lambda, \tag{2.41}$$

since this gives an exact match between upper and lower Ekman layer pumping and is therefore consistent with no normal (i.e. cross-contour) flow at the boundary. This is effectively a super-slip boundary condition (see Pedlosky, 1996), since the boundary value of ζ closely matches that on the upper slope, so the radial gradient of ζ nearly vanishes at the boundary. This boundary condition therefore results in a smooth radial variation of the azimuthal velocity, eliminating the lateral boundary layer.

Although most of the runs were conducted with the no-slip condition, it will be demonstrated in section 5.3 that the choice of boundary condition had no influence on the calculated flow in the sliced cone except in a very thin region in the immediate vicinity of $r = \Lambda$. This is because the velocity profile outside this thin lateral layer is very strongly controlled by a balance between Ekman friction and wind forcing, regardless of the lateral boundary condition.

2.3.3 Vorticity and energy integrals

Integrating the vorticity equation (2.33) over the domain and applying the Poisson equation (2.34), the kinematic boundary condition (2.38) and Gauss' and Green's theorems yields the equation

$$Ro\frac{\mathrm{d}\Gamma}{\mathrm{d}t} = 2\iint \mathfrak{E}\,\mathrm{d}A + E\oint \frac{\partial\zeta}{\partial r}\,\mathrm{d}S, \tag{2.42}$$

where

$$\Gamma = \iint \zeta\,\mathrm{d}A = \oint \frac{\partial\psi}{\partial r}\,\mathrm{d}S \tag{2.43}$$

is the circulation in the uppermost horizontal layer, and the line integrals are taken around the perimeter of the basin in the anticlockwise direction. Equation (2.42) demonstrates that the advection and orographic terms make no net contribution to the total vorticity balance, so this formulation conserves the integrated vorticity (i.e. the circulation) in the absence of viscosity.

Pedlosky (1996) discusses the role of boundary conditions in determining the basin-integrated vorticity balance. It is clear from (2.43) that the circulation is zero (and therefore independent of time) under the no-slip boundary condition (2.39), so there must be equal amounts of positive and negative vorticity in the basin in this case; as a result the Ekman friction vanishes from the integral balance if there is no bottom topography. Since the left-hand side and the Ekman friction vanish under the no-slip boundary condition in the limit of zero bottom topography, for the basin as a whole the vorticity input from the wind forcing is dissipated entirely by viscous diffusion through the lateral boundary. We expect this result to apply to a limited degree in the sliced cylinder since the depth variation is small, but the role of Ekman friction in the sliced cone with the no-slip condition may be much larger due to the $O(1)$ depth variation—this is discussed further in section 5.3.1. In contrast to the no-slip case, the lateral viscosity term makes no net contribution under the super-slip boundary condition and a steady flow must have an overall vorticity balance between wind forcing and Ekman friction.

Multiplying the vorticity equation (2.33) by ψ and integrating over the domain yields the energy equation

$$Ro\frac{\mathrm{d}K}{\mathrm{d}t} = -2\iint \psi\mathfrak{E}\,\mathrm{d}A - E\iint \psi\nabla_H^2\zeta\,\mathrm{d}A, \tag{2.44}$$

where

$$K = -\frac{1}{2}\iint \psi\zeta\,\mathrm{d}A \tag{2.45}$$

is the total horizontal kinetic energy per unit depth in the uppermost horizontal layer, given that we have chosen $\psi = 0$ on the boundary[6]. Note that the advection and orographic terms make no net contribution to the total energy balance, so this formulation conserves the total kinetic energy K in the absence of viscosity. Also note that a steady flow will have an energy balance between the Ekman and lateral viscosity terms.

2.4 Implementation of the numerical model

The numerical experiments were conducted using a modified version of a sliced cylinder code developed by Page (1982) and described in detail in his PhD thesis (Page, 1981). Page's algorithm is the same as that presented by Beardsley (1972), which was in turn based on the refinement by Israeli (1970) of a scheme proposed by Pearson (1965).

The code is a finite-difference method in polar coordinates. Spatial derivatives are calculated using second-order centred differences, except at the origin where a special flux-conserving integral treatment is used. The vorticity equation is advanced in time using the alternating-direction implicit method (Douglas, 1955; Peaceman & Rachford, 1955), which is unconditionally stable at zero Ro and therefore avoids stringent CFL-type restrictions due to the convergence of grid lines at the origin. A direct solver based on a fast Fourier transform in θ is used to solve the Poisson equation (2.34) for ψ. Since

[6]There is no simple expression for K in lower layers in the sliced cone, since ψ is not constant at the lateral boundary at a particular depth (i.e. the flow crosses the bounding depth contour).

the advective term in the vorticity equation couples it to (2.34), these two equations are solved iteratively within each timestep until both ψ and ζ converge (see figure 2.2). When the no-slip boundary condition (2.39) is used, this in-timestep iteration also serves to converge ζ at the boundary to a value which is consistent with this condition, using optimal relaxation. The complete algorithm is unconditionally stable for $Ro = 0$ (Page, 1982) and retains its stability for nonzero Ro provided the advective Courant number is less than one (Roache, 1982)[7]. The temporal scaling in the code is in terms of the Ekman spinup timescale rather than the advective timescale used in section 2.2, allowing the unsteady, linear adjustment to be studied.

For this application the code was modified to solve the vorticity equation (2.33) and include the effect of the sloping sidewalls on the bottom Ekman layer in the sliced cone. A large number of changes were made to the vorticity solver, the most important of which are listed below:

- eliminated $Ro\zeta\frac{\partial w}{\partial z}$ to make the formulation energy-conserving
- used conservative differencing for the advection and orographic terms to ensure that the finite-difference formulation retains the integral properties (2.42) and (2.44) (conservative differencing was already employed for the diffusion term)
- added an option to use the sliced cone topography
- implemented a novel differencing scheme for the orographic term (see equation (B.6)) which reduces flux errors due to the abrupt change in bottom slope at the join between the interior and sloping sidewall in the sliced cone
- changed the half-step at which the velocity is calculated so the flux components are evaluated at the same time
- added the correction to Ekman pumping on the sloping sidewall in the sliced cone
- added options for free-slip boundary conditions, and super-slip boundary conditions for the sliced cone
- solved the Poisson equation using the total ψ and ζ rather than their increments to avoid cumulative errors
- incorporated an algorithm to solve for unstable steady states (this is described in section 4.5).

An overview of the numerical scheme is shown in figure 2.2, and a detailed description of the vorticity equation solver is given in Appendix B. The Poisson solver and the method for solving the tridiagonal problems in the vorticity solver were retained as they were in Page's code (apart from a few efficiency improvements). Page's Poisson solver is described in Page (1981).

[7]However the advective term can become inaccurate at large Ro in strongly decelerating regions of the flow due to the use of second-order differences (Leonard, 1984). This effect was minimised by using high spatial resolution.

$n = 0$; initialise ζ^{n-1}, ψ^{n-1}, ζ^n and ψ^n
while $n \leq n_{max}$ **do**
  Guess $\widetilde{\zeta}^{n+\frac{1}{2}}$, $\widetilde{\psi}^{n+\frac{1}{2}}$, $\widetilde{\zeta}^{n+1}$ and $\widetilde{\psi}^{n+1}$ by linear extrapolation from steps $n-1$ and n
  repeat
    For no-slip boundary conditions, find correction $\check{\zeta}^{n+1}_{N_i,j}$ to $\widetilde{\zeta}^{n+1}_{N_i,j}$ by optimal relaxation
    Find correction $\check{\zeta}^{n+\frac{1}{2}}$ to $\widetilde{\zeta}^{n+\frac{1}{2}}$ in interior by solving the vorticity equation, evaluating θ differences at step $n+\frac{1}{2}$ and r differences at step n (see Appendix B.3.1)
    Set $\widetilde{\zeta}^{n+\frac{1}{2}} \leftarrow \widetilde{\zeta}^{n+\frac{1}{2}} + \check{\zeta}^{n+\frac{1}{2}}$
    Find correction $\check{\zeta}^{n+1}$ to $\widetilde{\zeta}^{n+1}$ in interior by solving the vorticity equation, evaluating θ differences at step $n+\frac{1}{2}$ and r differences at step $n+1$ (see Appendix B.3.2)
    Set $\widetilde{\zeta}^{n+1} \leftarrow \widetilde{\zeta}^{n+1} + \check{\zeta}^{n+1}$
    Obtain the corrected $\widetilde{\psi}^{n+1}$ by solving the Poisson equation (2.34) using the corrected $\widetilde{\zeta}^{n+1}$, and use this to update $\widetilde{\psi}^{n+\frac{1}{2}}$
  until the corrections $\check{\zeta}^{n+1}$ and $\check{\psi}^{n+1}$ are negligible
  Set $n \leftarrow n+1$
end while

Figure 2.2: Overview of the numerical scheme, based on the alternating-direction implicit method. Tildes denote approximate values and inverted "hats" indicate corrections. Superscripts are timesteps, and subscripts are grid locations (i is the radial index, $0 < i < N_i$, and j is the azimuthal index, $1 < j < N_j$). Details are given in Appendix B.